



## COMMUNICATION

[View Article Online](#)  
[View Journal](#) | [View Issue](#)Cite this: *J. Mater. Chem. A*, 2022, 10, 5930Received 18th September 2021  
Accepted 9th November 2021

DOI: 10.1039/d1ta08029f

[rsc.li/materials-a](https://rsc.li/materials-a)

## Nitrogen-coordinated single-atom catalysts with manganese and cobalt sites for acidic oxygen reduction†

Guojie Chao,<sup>a</sup> Yizhe Zhang,<sup>a</sup> Longsheng Zhang,<sup>\*a</sup> Wei Zong,<sup>b</sup> Nan Zhang,<sup>a</sup> Tiantian Xue,<sup>b</sup> Wei Fan,<sup>b</sup>  Tianxi Liu<sup>a</sup> and Yi Xie  <sup>\*c</sup>

Developing a low-cost, highly active and durable catalyst for acidic oxygen reduction reaction (ORR) is of significant importance for proton-exchange electrolyte membrane fuel cell. In this work, we report an efficient catalyst based on Mn, Co and N co-doped carbon (MnCo–N–C) for acidic ORR. Electron microscopy and X-ray absorption spectroscopy indicate that atomic CoN<sub>x</sub> and MnN<sub>x</sub> sites are dispersed in the carbon matrices of MnCo–N–C. Raman spectroscopy verifies that the doping of Mn into carbon matrices can enable a higher graphitization degree, which can improve the corrosion resistance and catalytic durability of the MnCo–N–C catalyst towards ORR in challenging acidic media. As a result, the MnCo–N–C catalyst exhibits significantly improved ORR durability with a higher current retention of 81% after 50 h of test compared with that (52%) of the Co–N–C catalyst. Moreover, the half-wave potential of the MnCo–N–C catalyst increases by 100 mV compared with that of the Co–N–C catalyst.

## Introduction

Challenges from the growing global energy demand provide a strong driving force for the rapid advancement of efficient conversion of renewable energy.<sup>1</sup> Among others, proton-exchange electrolyte membrane fuel cells (PEMFCs) can convert renewable and carbon-free hydrogen energy into electricity, and have shown potential applications in portable electronic devices, electric vehicles and stationary power sources.<sup>2</sup> One of the biggest issues in achieving the large-scale

application of PEMFCs is to develop alternative catalysts to platinum group metal (PGM) catalysts for the sluggish oxygen reduction reaction (ORR) in acidic electrolytes.<sup>3–5</sup>

Great efforts have been devoted to developing cost-effective, highly active and durable PGM-free catalysts for acidic ORR. Recently, a class of transition metals (Fe, Co, Mn, Cu, *etc.*) and N co-doped carbon (denoted as M–N–C) catalysts have received extensive attention due to their maximum atom-utilization efficiencies and encouraging performance towards acidic ORR.<sup>6–10</sup> To date, compared to other M–N–C catalysts, the Fe–N–C catalyst has shown the highest catalytic activity, which is close to those of PGM catalysts towards acidic ORR.<sup>11–13</sup> However, inevitable Fenton reactions between the generated H<sub>2</sub>O<sub>2</sub> and dissolved Fe ions during the ORR process will produce hydroxyl and hydroperoxyl radical species, which would lead to fast degradation of ionomers and membranes in PEMFCs.<sup>14,15</sup> Thus, the exploration of Fe-free alternative M–N–C catalysts that can barely induce Fenton reactions is desired for achieving durable and inexpensive PEMFCs.

Previous studies have illustrated that the catalytic activity of M–N–C catalysts follows the order of Fe > Co > Mn > Cu > Ni towards acidic ORR.<sup>16,17</sup> Compared with Fe ions, Co ions are much less active in initiating Fenton reactions,<sup>18</sup> making Co–N–C catalysts good candidates for Fe-free and PGM-free catalysts for acidic ORR. However, Co–N–C catalysts suffer from an undesired two-electron pathway during the acidic ORR process and generate substantial amounts of H<sub>2</sub>O<sub>2</sub>, which would induce H<sub>2</sub>O<sub>2</sub> oxidative attacks on the catalysts and thereby lead to serious dissolution of active metal sites.<sup>19,20</sup> Besides, carbon corrosion of catalysts in challenging acidic media would also promote the dissolution of active metal sites followed by catalyst degradation.<sup>21</sup> Concomitantly, corroded carbon matrices with active oxygenated groups would induce a two-electron pathway and generate undesired H<sub>2</sub>O<sub>2</sub> during the ORR process, which would accelerate the catalyst degradation.<sup>22</sup> Recent studies have shown that introducing Mn into the carbon matrices of M–N–C catalysts can increase the degree of graphitization of carbon matrices, which is of great significance to

<sup>a</sup>Key Laboratory of Synthetic and Biological Colloids, Ministry of Education, School of Chemical and Material Engineering, International Joint Research Laboratory for Nano Energy Composites, Jiangnan University, Wuxi, China. E-mail: zhangls@jiangnan.edu.cn

<sup>b</sup>State Key Laboratory for Modification of Chemical Fibers and Polymer Materials, College of Materials Science and Engineering, Donghua University, Shanghai, China

<sup>c</sup>Hefei National Laboratory for Physical Sciences at Microscale, University of Science and Technology of China, Hefei, China. E-mail: yxie@ustc.edu.cn

† Electronic supplementary information (ESI) available. See DOI: 10.1039/d1ta08029f

enhance the corrosion resistance of carbon matrices.<sup>23</sup> Meanwhile, it was reported that Mn ions are hardly involved in Fenton reactions due to the weak reaction activity between Mn ions and H<sub>2</sub>O<sub>2</sub> species.<sup>24</sup> We posit that doping Mn in carbon matrices of Co–N–C may catalyze the graphitic structures and improve the ORR stability of Co–N–C, so as to obtain ORR catalysts with both high activity and durability in acidic electrolytes.

Here, we report a Mn, Co and N co-doped carbon (MnCo–N–C) catalyst for acidic ORR, which can be synthesized *via* a facile method based on zeolitic imidazolate frameworks. Owing to their high specific surface area and abundant nitrogen sources, zeolitic imidazolate frameworks were thereby chosen as precursors for preparing the MnCo–N–C catalyst in this work. Our extensive characterization reveals that the configurations of atomic CoN<sub>x</sub> and MnN<sub>x</sub> sites are well embedded in the carbon matrices of the MnCo–N–C catalyst. Raman spectroscopy indicates that the doping of Mn into carbon matrices can induce a higher graphitization degree, thus improving the corrosion resistance of MnCo–N–C compared with that of Co–N–C. As a consequence, the MnCo–N–C catalyst exhibits greatly enhanced ORR durability with a current density retention of 81% over 50 h of continuous test, much higher than that (52%) of Co–N–C catalyst. Moreover, the MnCo–N–C catalyst shows

a higher half-wave potential ( $E_{1/2}$ ) of 0.80 V (*vs.* the reversible hydrogen electrode, RHE), compared to that (0.70 V *vs.* RHE) of Co–N–C catalyst. Furthermore, a small negative shift of 25 mV in  $E_{1/2}$  is achieved for MnCo–N–C catalyst after 5000 cycles of accelerated durability tests, in contrast to that (90 mV) of Co–N–C catalyst.

## Results and discussion

As illustrated in Fig. S1,<sup>†</sup> the MnCo–N–C sample was obtained by carbonizing the Mn and Co co-doped zeolitic imidazolate framework (see synthesis details in the ESI<sup>†</sup>). As shown in the scanning electron microscopy (SEM) image (Fig. 1a), the MnCo–N–C sample shows a rhombododecahedral morphology with a size of 300–400 nm. Transmission electron microscopy (TEM) and energy-dispersive elemental mapping images reveal that Co, Mn, N and C elements are homogeneously distributed within the MnCo–N–C sample (Fig. 1b and c). High angle annular dark-field scanning transmission electron microscopy (HAADF-STEM) was further performed to obtain evidence of the Co and Mn distribution with atomic resolution (Fig. 1d). Small bright spots can be observed in the carbon matrices, indicating the configuration of single-metal sites in the

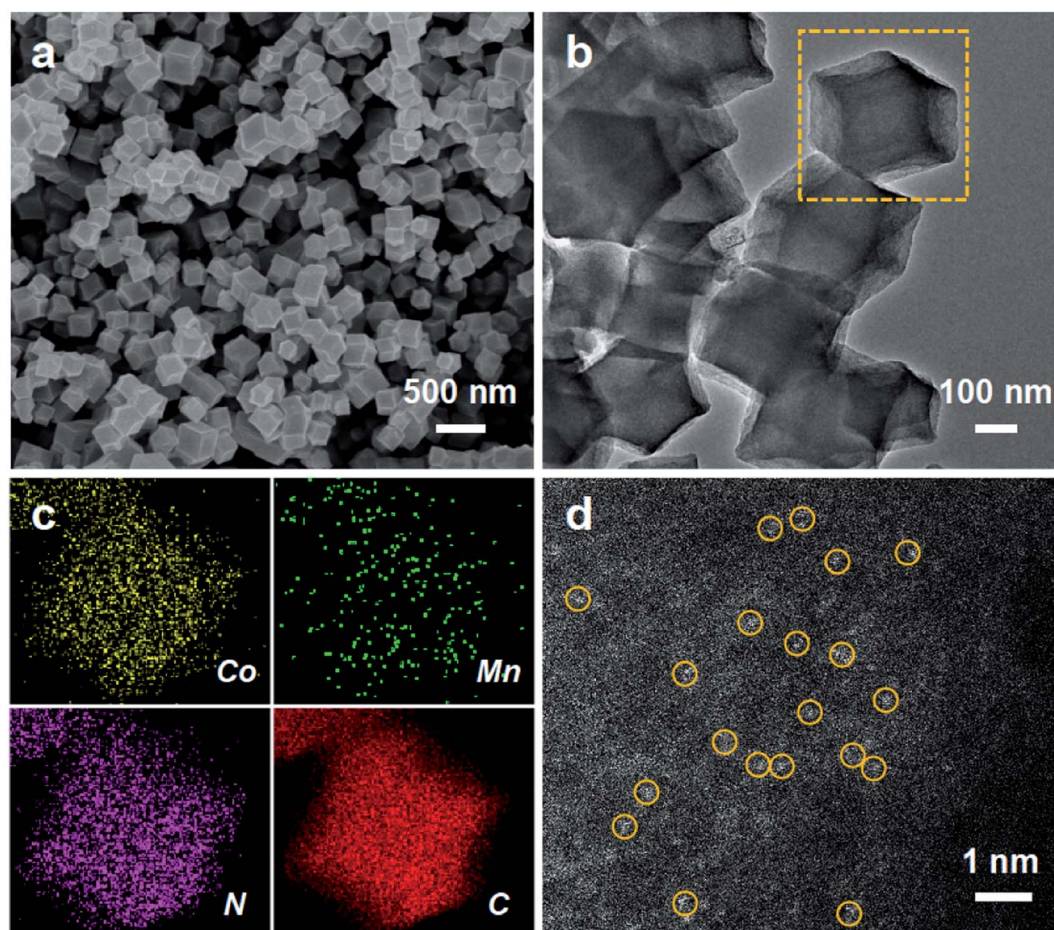


Fig. 1 Morphology characterization of MnCo–N–C sample. (a) SEM image. (b and c) TEM and corresponding element mapping images, respectively. (d) HAADF-STEM image.

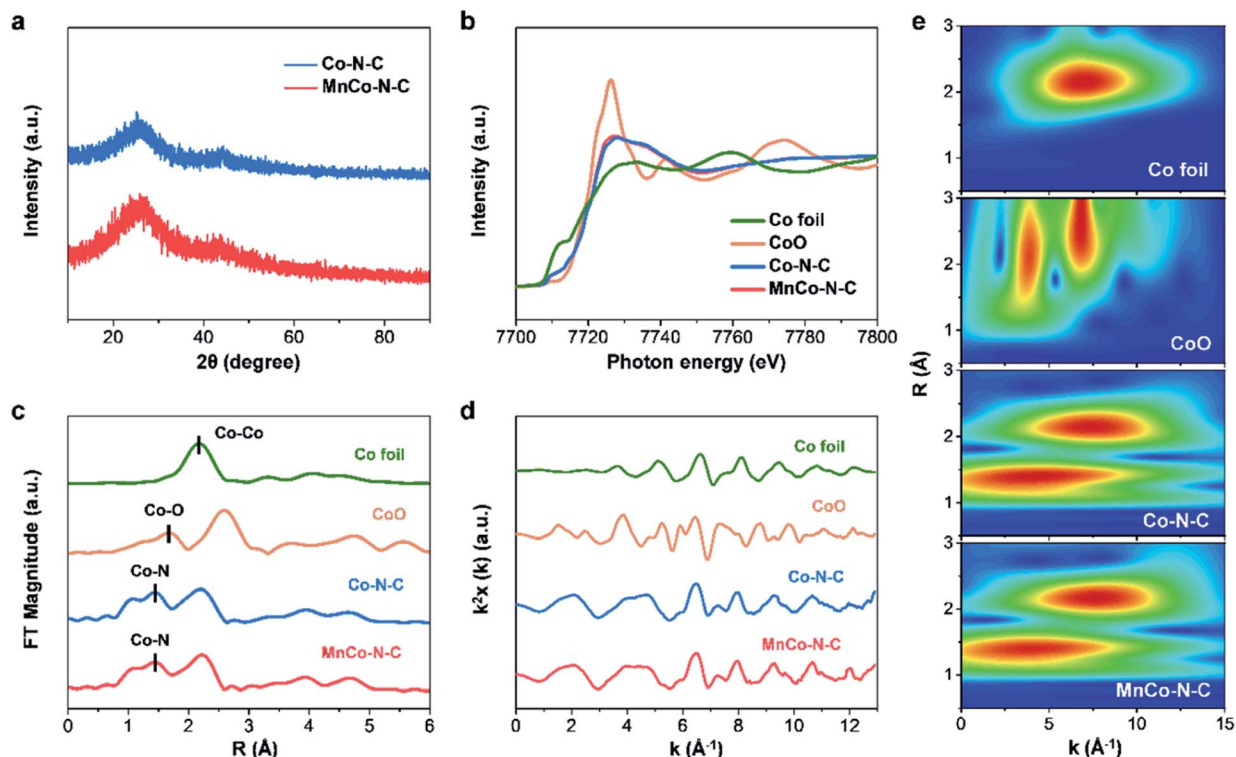


Fig. 2 Structural characterization of MnCo-N-C and controls. (a) XRD patterns. (b and c) Co K-edge XANES and EXAFS spectra, respectively. (d and e)  $k^2$ -weighted XAFS  $\chi(k)$  and wavelet transform, respectively.

MnCo-N-C sample. Most of the Mn and Co atoms exist separately during the formation of Co-N-C and Mn-N-C structures, and a few Mn and Co atoms exist as diatomic pairs. The contents of Mn and Co in the MnCo-N-C sample are 0.6 and 1.0 wt%, respectively (Table S1†). As shown in Fig. 2a, the X-ray diffraction (XRD) patterns of the MnCo-N-C sample and controls demonstrate that only two diffraction peaks of graphitic carbon are observed and no diffraction peaks of metals or oxides are found.

To further get the coordination information of Co for MnCo-N-C and controls, we carried out X-ray absorption near-edge structure (XANES) and extended X-ray absorption fine structure (EXAFS) measurements. The Co K-edge XANES spectra show that the adsorption threshold positions of the two Co-doped M-N-C samples are located between Co foil and CoO (Fig. 2b), which illustrate that the valences of Co species in these two samples are situated between 0 and +2. The Fourier transform  $k^2$ -weighted EXAFS spectra of Co-N-C and MnCo-N-C (Fig. 2c) show similar peaks at 1.43 Å, which are much shorter than the Co-O peak of the CoO reference at 1.67 Å and can be assigned to the Co-N contributions. In addition, the electron energy loss spectrum (Fig. S2†) illustrates that both N and Co elements exist in the MnCo-N-C sample, indicating that Co is coordinated with N at the atomic scale.<sup>6,26</sup> Besides, the peaks observed at 2.22 Å for the Co-N-C and MnCo-N-C samples indicate the existence of Co clusters or nanoparticles. Since Co clusters or nanoparticles are inactive for the ORR,<sup>25–27</sup> this study mainly focuses on nitrogen-coordinated single-atom Co sites

(Co-N-C) with catalytic activity towards the ORR. The Fourier transform  $k^2$ -weighted XAFS  $\chi$  versus the reciprocal wave vector (Fig. 2d) indicates good qualities of the EXAFS data. Wavelet transform was further used to investigate the EXAFS oscillations of the samples. The wavelet transform analysis of both Co-N-C and MnCo-N-C catalysts shows intensity maxima at approximately 1.4 Å ( $k = 3 \text{ Å}^{-1}$ ,  $R = 1.4 \text{ Å}$ ), which can be attributed to Co-N contributions (Fig. 2e), verifying the formation of CoN<sub>x</sub> sites.

X-ray photoelectron spectroscopy (XPS) measurements were further performed to reveal the chemical composition and states of MnCo-N-C and controls. As shown in the high-resolution N 1s spectra of Co-N-C and MnCo-N-C (Fig. 3a and b), the fitted spectra have four types of N species, attributed to graphitic N, pyrrolic N, metal-N and pyridinic N, respectively. The metal-N species of MnCo-N-C can be associated with the atomically dispersed CoN<sub>x</sub> and MnN<sub>x</sub> moieties. Table S2† shows the contents of these four types of N species in samples, obtained from the fitting of XPS results. Note that the content of metal-N species in the MnCo-N-C catalyst (32.0%) is much higher than that of the Co-N-C catalyst (19.6%), which can be ascribed to MnN<sub>x</sub> and CoN<sub>x</sub> moieties in the MnCo-N-C catalyst. As shown in Fig. 3c and d, the high-resolution Co 2p spectra of MnCo-N-C and controls indicate the existence of CoN<sub>x</sub> and metallic Co species, in agreement with the EXAFS analysis. The high-resolution Mn 2p spectrum of the MnCo-N-C catalyst reveals that the Mn 2p<sub>1/2</sub> peak (654.0 eV) and Mn 2p<sub>3/2</sub> peak (642.0 eV) can be ascribed to the MnN<sub>x</sub> moieties (Fig. 3e), in



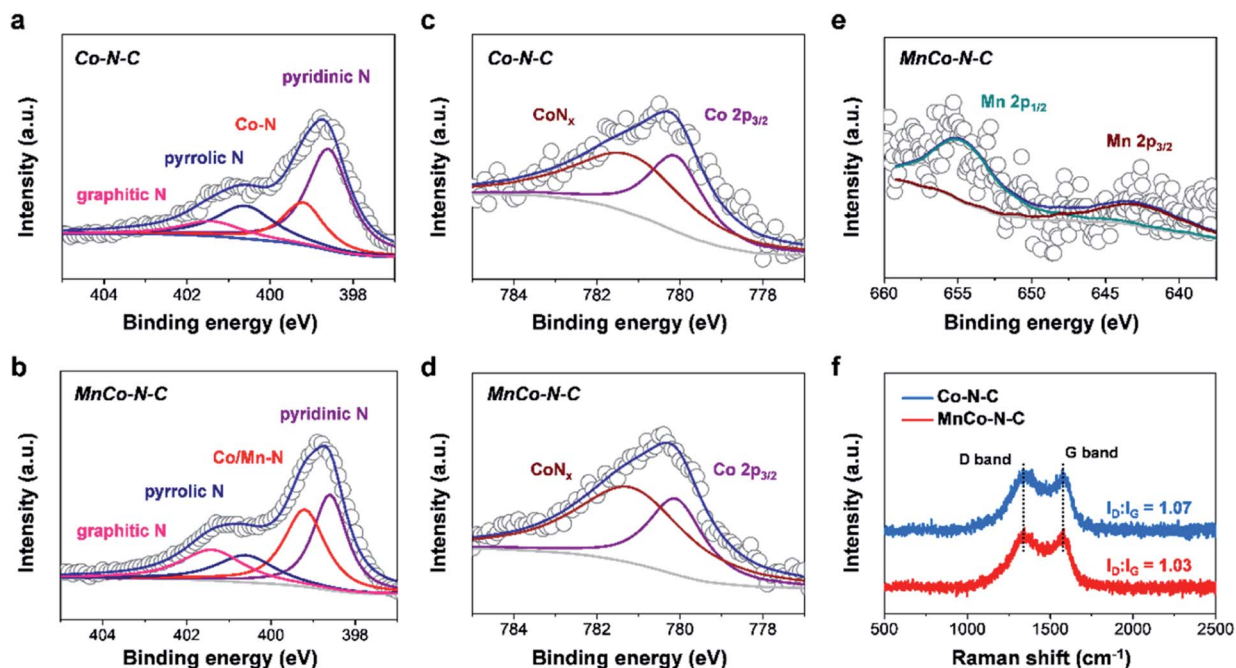


Fig. 3 Structural characterization of MnCo-N-C and controls. High-resolution (a and b) N 1s spectra, (c and d) Co 2p spectra and (e) Mn 2p spectrum, respectively. (f) Raman spectra.

accordance with those of previously-reported Mn-N-C catalysts.<sup>6,28</sup> Compared with the Mn-N-C catalyst, the XPS peaks of Mn 2p of the MnCo-N-C catalyst show a positive shift of  $\sim 0.9$  eV (Fig. S3†), which may be ascribed to the interaction between Mn atoms and Co atoms. Raman measurements were conducted to further investigate the influence of Mn doping on the graphitization degree of carbon matrices. As shown in Fig. 3f and S4,† the Raman spectra of all the samples exhibit two peaks at 1354 and 1591  $\text{cm}^{-1}$ , which are respectively indexed to disordered  $\text{sp}^3$  carbon (D band) and graphitic  $\text{sp}^2$  carbon (G band). The D and G band intensity ratio of MnCo-N-C is lower than that of Co-N-C, verifying the higher graphitization degree of carbon matrices with Mn dopants.<sup>29,30</sup> As reported, the doping of Mn into carbon matrices can induce the formation of ordered graphitic carbon with fewer defects and thus result in a higher graphitization degree.<sup>23</sup>  $\text{N}_2$  adsorption-desorption measurements (Fig. S5†) show that both Co-N-C and MnCo-N-C samples show mesopores and the specific surface areas of Co-N-C and MnCo-N-C samples are 506 and 420  $\text{m}^2 \text{g}^{-1}$ , respectively.

The electrochemical measurements of MnCo-N-C and controls were carried out to evaluate their ORR activities in acidic media. As shown in Fig. S6,† obvious reduction peaks are observed in the cyclic voltammetry (CV) curves of catalysts measured in  $\text{O}_2$ -saturated media in contrast to those in  $\text{N}_2$ -saturated media. Notably, compared with Co-N-C, the reduction peak of MnCo-N-C is more positive (Fig. 4a), suggesting its higher activity towards the ORR. Linear sweep voltammetry (LSV) was further performed to assess their ORR activities (Fig. 4b, S7 and S8†). The  $E_{1/2}$  (0.80 V vs. RHE) of MnCo-N-C is comparable to that (0.86 V vs. RHE) of Pt/C, which is higher than

that (0.70 V vs. RHE) of Co-N-C and that (0.50 V vs. RHE) of Mn-N-C. As shown in Fig. S9,† by normalizing the obtained currents to the specific surface areas from the  $\text{N}_2$  adsorption-desorption analysis, the specific activities of the MnCo-N-C catalyst are found to be higher than those of the Co-N-C catalyst at various potentials. Besides, the MnCo-N-C sample has a smaller Tafel slope (Fig. S10†), indicating its faster kinetics towards the ORR. The electrochemical selectivity of the catalyst was further studied through rotating ring disk electrode (RRDE) polarization tests (Fig. 4c, S11 and S12†). Compared with the Co-N-C catalyst, the electron transfer number of the MnCo-N-C catalyst is close to 4 and the  $\text{H}_2\text{O}_2$  yield of the MnCo-N-C catalyst is lower, indicating its higher selectivity over the four-electron reaction pathway towards the ORR.

The catalytic durability of MnCo-N-C and controls in acidic media was evaluated *via* current-time chronoamperometry (*i*-t) and accelerated durability tests (ADT). During the *i*-t experiment (Fig. 4d), MnCo-N-C shows a much higher current retention of 81% after continuous operation for 50 h, in comparison with that (52%) of Co-N-C. In challenging acidic electrolytes, corrosion of carbon matrices of the MnCo-N-C catalyst can be mitigated to some extent, which is still inevitable and can not be totally avoided. Besides, the undesired  $\text{H}_2\text{O}_2$  that is generated during the ORR process would induce oxidative attacks on the MnCo-N-C catalyst and thereby cause dissolution of active metal sites.<sup>7,15</sup> These observations would result in the performance decay of the MnCo-N-C catalyst with increase of time during the long-term ORR test. Moreover, MnCo-N-C exhibits good durability during the ADT experiment (Fig. 4e and f). After 5000 cycles, the  $E_{1/2}$  of MnCo-N-C exhibits a small negative shift of 25 mV, while the  $E_{1/2}$  of Co-N-C exhibits



Fig. 4 Electrochemical measurements of MnCo-N-C and controls. (a and b) CV and LSV curves obtained in O<sub>2</sub>-saturated electrolytes, respectively. (c) Electron transfer number ( $n$ ) and H<sub>2</sub>O<sub>2</sub> yield ( $y$ ), and (d) the  $i$ - $t$  experiments of catalysts, respectively. (e and f) LSV curves of catalysts before and after 5000 cycles of tests, respectively.

a rapid decay with a negative shift of 90 mV. These results, taken together, demonstrate that MnCo-N-C exhibits high catalytic activity, selectivity and durability towards the ORR in the challenging acidic media. Moreover, MnCo-N-C also exhibits superior methanol tolerance and excellent basic ORR performance (Fig. S13<sup>†</sup>). As shown in Fig. S14<sup>†</sup>, the LSV curves of MnCo-N-C and Pt/C catalysts obtained in O<sub>2</sub>-saturated 0.1 M KOH aqueous electrolytes reveal that the half-wave potential (0.89 V vs. RHE) of the MnCo-N-C catalyst is higher than that (0.84 V vs. RHE) of the commercial Pt/C catalyst, indicating its good ORR performance in alkaline electrolytes.

To further understand the ORR process on the surface of Co-N-C and MnCo-N-C, *in situ* ATR-SEIRAS measurements were further carried out (Fig. 5 and S15<sup>†</sup>). The ATR-SEIRAS spectra of these two catalysts show a vibration peak located at  $\nu = 1020$  cm<sup>-1</sup> that becomes more pronounced as the experiments proceed, which can be ascribed to the \*O<sub>2</sub><sup>-</sup> intermediate.<sup>31–33</sup> As clearly observed, the vibration peak of the \*O<sub>2</sub><sup>-</sup> intermediate becomes much stronger for Co-N-C than that of MnCo-N-C. Besides, compared with the Co-N-C catalyst, stronger vibration

peaks of the \*OOH intermediate at  $\nu = 1212$  cm<sup>-1</sup> are observed in the spectra of the MnCo-N-C catalyst.<sup>33</sup> As reported, during the ORR process, the selectivity for electroreduction of O<sub>2</sub> to H<sub>2</sub>O<sub>2</sub> (via the two-electron reaction pathway) or H<sub>2</sub>O (via the four-electron reaction pathway) is mainly determined by its propensity to break the O–O bond. The strong binding of \*OOH intermediates on the catalyst surface will result in the predominance of the four-electron pathway over the two-electron pathway, which causes the \*OOH intermediates to be reduced and dissociate into \*O and \*OH intermediates, thereby enabling electroreduction of O<sub>2</sub> to H<sub>2</sub>O.<sup>19,34</sup> By contrast, the strong binding of \*O<sub>2</sub><sup>-</sup> intermediates on the catalyst surface will shift the reaction mechanism to follow the two-electron reaction pathway to generate H<sub>2</sub>O<sub>2</sub> (\*O<sub>2</sub><sup>-</sup> + 2H<sup>+</sup> + e<sup>-</sup> → H<sub>2</sub>O<sub>2</sub>) during the ORR process.<sup>31,33</sup> The faster kinetics of \*OOH formation and adsorbed \*O<sub>2</sub><sup>-</sup> desorption of the MnCo-N-C catalyst can correlate well with its enhanced activity and selectivity towards the ORR. The lower yield of H<sub>2</sub>O<sub>2</sub> of the MnCo-N-C catalyst during the ORR process would enable less H<sub>2</sub>O<sub>2</sub> oxidative attacks on the catalyst and enhance the durability of the MnCo-N-C catalyst.



Fig. 5 (a and b) *In situ* ATR-SEIRAS spectra of Co-N-C and MnCo-N-C, respectively.

## Conclusions

In summary, we demonstrate a novel design of acidic ORR catalyst by co-doping Mn, Co and N into carbon matrices, and the resultant MnCo-N-C catalyst shows greatly boosted activity, selectivity and durability compared with the Co-N-C catalyst. The HAADF-STEM, XAFS and XPS studies indicate that CoN<sub>x</sub> and MnN<sub>x</sub> atomic sites are dispersed in the carbon matrices of the MnCo-N-C catalyst. Besides, the Raman spectroscopy results verify that the doping of Mn can improve the graphitization of carbon matrices, thus enhancing the corrosion resistance and catalytic durability of the MnCo-N-C catalyst. The formation of ordered graphitic carbon with less active oxygenated groups can decrease the yield of H<sub>2</sub>O<sub>2</sub> during the ORR process, which can decrease the undesired oxidative attacks on the catalyst and in turn promote the durability of the MnCo-N-C catalyst. This work provides insights for further advances in the development of high-performance acidic ORR catalysts for PEMFCs.

## Conflicts of interest

There are no conflicts to declare.

## Acknowledgements

This work was financially supported by the Fundamental Research Funds for the Central Universities (2232019A3-03, and JUSRP121035), National Natural Science Foundation of China

(21875033, and 52103260), China Postdoctoral Science Foundation (2021M690067), Natural Science Foundation of Jiangsu Province for Youths (BK20210482) and Jiangsu Province Postdoctoral Science Foundation (2021K053A).

## References

- 1 X. X. Wang, M. T. Swihart and G. Wu, *Nat. Catal.*, 2019, **2**, 578–589.
- 2 L. Chong, J. G. Wen, J. Kubal, F. G. Sen, J. X. Zou, J. Greeley, M. Chan, H. Barkholtz, W. J. Ding and D. J. Liu, *Science*, 2018, **362**, 1276–1281.
- 3 Y. X. Wang, X. Z. Cui, L. W. Peng, L. L. Li, J. L. Qiao, H. T. Huang and J. L. Shi, *Adv. Mater.*, 2021, **33**, 2100997.
- 4 H. Cheng, R. J. Gui, H. Yu, C. Wang, S. Liu, H. F. Liu, T. P. Zhou, N. Zhang, X. S. Zheng, W. S. Chu, Y. Lin, H. A. Wu, C. Z. Wu and Y. Xie, *Proc. Natl. Acad. Sci. U. S. A.*, 2021, **118**, e2104026118.
- 5 G. J. Chao, X. Y. An, L. S. Zhang, J. Tian, W. Fan and T. X. Liu, *Compos. Commun.*, 2021, **24**, 100603.
- 6 X. H. Xie, C. He, B. Y. Li, Y. H. He, D. A. Cullen, E. C. Wegener, A. J. Kropf, U. Martinez, Y. W. Cheng, M. H. Engelhard, M. E. Bowden, M. Song, T. Lemmon, X. S. Li, Z. M. Nie, J. Liu, D. J. Myers, P. Zelenay, G. F. Wang, G. Wu, V. Ramani and Y. Y. Shao, *Nat. Catal.*, 2020, **3**, 1044–1054.
- 7 J. Z. Li, M. J. Chen, D. A. Cullen, S. Hwang, M. Y. Wang, B. Y. Li, K. X. Liu, S. Karakalos, M. Lucero, H. G. Zhang, C. Lei, H. Xu, G. E. Sterbinsky, Z. X. Feng, D. Su, K. L. More, G. F. Wang, Z. B. Wang and G. Wu, *Nat. Catal.*, 2018, **1**, 935–945.
- 8 F. Li, G. F. Han, H. J. Noh, S. J. Kim, Y. L. Lu, H. Y. Jeong, Z. P. Fu and J. B. Baek, *Energy Environ. Sci.*, 2018, **11**, 2263–2269.
- 9 J. K. Li, M. T. Sougrati, A. Zitolo, J. M. Ablett, I. C. Oguz, T. Mineva, I. Matanovic, P. Atanassov, Y. Huang, I. Zenyuk, A. Di Cicco, K. Kumar, L. Dubau, F. Maillard, G. Drazic and F. Jaouen, *Nat. Catal.*, 2021, **4**, 10–19.
- 10 E. G. Luo, H. Zhang, X. Wang, L. Q. Gao, L. Y. Gong, T. Zhao, Z. Jin, J. J. Ge, Z. Jiang, C. P. Liu and W. Xing, *Angew. Chem., Int. Ed.*, 2019, **58**, 12469–12475.
- 11 Y. H. He, S. Hwang, D. A. Cullen, M. A. Uddin, L. Langhorst, B. Y. Li, S. Karakalos, A. J. Kropf, E. C. Wegener, J. Sokolowski, M. J. Chen, D. Myers, D. Su, K. L. More, G. F. Wang, S. Litster and G. Wu, *Energy Environ. Sci.*, 2019, **12**, 250–260.
- 12 H. T. Chung, D. A. Cullen, D. Higgins, B. T. Sneed, E. F. Holby, K. L. More and P. Zelenay, *Science*, 2017, **357**, 479–483.
- 13 H. G. Zhang, S. Hwang, M. Y. Wang, Z. X. Feng, S. Karakalos, L. L. Luo, Z. Qiao, X. H. Xie, C. M. Wang, D. Su, Y. Y. Shao and G. Wu, *J. Am. Chem. Soc.*, 2017, **139**, 14143–14149.
- 14 C. H. Choi, H. K. Lim, M. W. Chung, G. Chon, N. R. Sahraie, A. Altin, M. T. Sougrati, L. Stievano, H. S. Oh, E. S. Park, F. Luo, P. Strasser, G. Drazic, K. J. J. Mayrhofer, H. Kim and F. Jaouen, *Energy Environ. Sci.*, 2018, **11**, 3176–3182.

- 15 X. X. Wang, V. Prabhakaran, Y. H. He, Y. Y. Shao and G. Wu, *Adv. Mater.*, 2019, **31**, 1805126.
- 16 H. L. Peng, F. F. Liu, X. J. Liu, S. J. Liao, C. H. You, X. L. Tian, H. X. Nan, F. Luo, H. Y. Song, Z. Y. Fu and P. Y. Huang, *ACS Catal.*, 2014, **4**, 3797–3805.
- 17 J. Masa, A. Q. Zhao, W. Xia, M. Muhler and W. Schuhmann, *Electrochim. Acta*, 2014, **128**, 271–278.
- 18 S. T. Thompson, A. R. Wilson, P. Zelenay, D. J. Myers, K. L. More, K. C. Neyerlin and D. Papageorgopoulos, *Solid State Ionics*, 2018, **319**, 68–76.
- 19 Y. Y. Sun, L. Silvioli, N. R. Sahraie, W. Ju, J. K. Li, A. Zitolo, S. Li, A. Bagger, L. Arnarson, X. L. Wang, T. Moeller, D. Bernsmeier, J. Rossmeisl, F. Jaouen and P. Strasser, *J. Am. Chem. Soc.*, 2019, **141**, 12372–12381.
- 20 D. Banham, S. Ye, K. Pei, J. Ozaki, T. Kishimoto and Y. Imashiro, *J. Power Sources*, 2015, **285**, 334–348.
- 21 C. H. Choi, C. Baldizzone, J. P. Grote, A. K. Schuppert, F. Jaouen and K. J. J. Mayrhofer, *Angew. Chem., Int. Ed.*, 2015, **54**, 12753–12757.
- 22 B. Q. Li, C. X. Zhao, J. N. Liu and Q. Zhang, *Adv. Mater.*, 2019, **31**, 1808173.
- 23 S. Gupta, S. Zhao, X. X. Wang, S. Hwang, S. Karakalos, S. V. Devaguptapu, S. Mukherjee, D. Su, H. Xu and G. Wu, *ACS Catal.*, 2017, **7**, 8386–8393.
- 24 Y. H. Zhong, X. L. Liang, Z. S. He, W. Tan, J. X. Zhu, P. Yuan, R. L. Zhu and H. P. He, *Appl. Catal., B*, 2014, **150–151**, 612–618.
- 25 G. G. Yang, J. W. Zhu, P. F. Yuan, Y. F. Hu, G. Qu, B. A. Lu, X. Y. Xue, H. B. Yin, W. Z. Cheng, J. Q. Cheng, W. J. Xu, J. Li, J. S. Hu, S. C. Mu and J. N. Zhang, *Nat. Commun.*, 2021, **12**, 1734.
- 26 X. X. Wang, D. A. Cullen, Y. T. Pan, S. Hwang, M. Y. Wang, Z. X. Feng, J. Y. Wang, M. H. Engelhard, H. G. Zhang, Y. H. He, Y. Y. Shao, D. Su, K. L. More, J. S. Spendelow and G. Wu, *Adv. Mater.*, 2018, **30**, 1706758.
- 27 B. You, N. Jiang, M. L. Sheng, W. S. Drisdell, J. Yano and Y. J. Sun, *ACS Catal.*, 2015, **5**, 7068–7076.
- 28 S. C. Sun, G. Q. Shen, J. W. Jiang, W. B. Mi, X. L. Liu, L. Pan, X. W. Zhang and J. J. Zou, *Adv. Energy Mater.*, 2019, **9**, 1901505.
- 29 G. J. Chao, L. S. Zhang, J. Tian, W. Fan and T. X. Liu, *Compos. Commun.*, 2021, **25**, 100703.
- 30 T. Y. Zhu, Q. C. Feng, S. L. Liu and C. Zhang, *Compos. Commun.*, 2020, **20**, 100376.
- 31 S. Nayak, P. U. Biedermann, M. Stratmann and A. Erbe, *Electrochim. Acta*, 2013, **106**, 472–482.
- 32 S. Nayak, I. J. McPherson and K. A. Vincent, *Angew. Chem., Int. Ed.*, 2018, **57**, 12855–12858.
- 33 Y. Y. Wang, D. J. Chen, T. C. Allison and Y. Y. J. Tong, *J. Chem. Phys.*, 2019, **150**, 041728.
- 34 S. Siahrostami, A. Verdager-Casadevall, M. Karamad, D. Deiana, P. Malacrida, B. Wickman, M. Escudero-Escribano, E. A. Paoli, R. Frydendal, T. W. Hansen, I. Chorkendorff, I. E. L. Stephens and J. Rossmeisl, *Nat. Mater.*, 2013, **12**, 1137–1143.